JOURNAL OF MATERIALS SCIENCE **37** (2002) 1547–1555

In-situ deformation of an open-cell flexible polyurethane foam characterised by 3D computed microtomography

J. A. ELLIOTT, A. H. WINDLE
Department of Materials Science and Metallurgy, University of Cambridge, Pembroke Street, Cambridge, CB2 3QZ, UK
E-mail: jae1001@cam.ac.uk

J. R. HOBDELL, G. EECKHAUT
Huntsman Corporation, Everslaan 45, B-3078 Everberg, Belgium

R. J. OLDMAN
ICI Technology, The Heath, Runcorn, Cheshire WA7 4QD, UK

W. LUDWIG, E. BOLLER, P. CLOETENS, J. BARUCHEL
ESRF, BP 220, F-38043 Grenoble Cedex, France

The deformation behaviour of an open-cell flexible polyurethane foam was observed using X-ray microtomography on the ID19 beamline at the ESRF in Grenoble, France. Tomographs, consisting of 1024 voxels cubed, were collected with a voxel size of 6.6 μm from a small region near the centre of the foam at a range of compressive strains between 0 and 80%. The results show that the initial stages of compression are taken up by small amounts of elastic bending in struts that are inclined to the compression direction. At 23% strain, entirely collapsed bands were observed in the structure. By 63% strain, there was evidence of struts impinging on each other, corresponding to the densification regime. The compression of an irregular foam (i.e. one with strut length and cell size distributions) appears to involve a sudden change in modulus, accompanied by localised increases in density. Observations of this nature would have been extremely difficult to interpret unambiguously without the ability to carry out sequential microtomographic imaging under realistic *in situ* loading conditions. The process of finite element analysis (FEA) was begun by constructing node-strut models from the experimental data by a mathematical skeletonisation process. These were used to derive node coordination, strut-length and cell-size distributions. However, direct comparison of the elastic properties with FEA was hampered by the absence of periodicity in the experimentally determined foam structures.

1. Introduction

1.1. Open-cell flexible foams and their mechanical behaviour

Open-cell flexible foams are industrially important materials with widespread use in household furniture and car seating. The cushioning application of these materials depends critically on how they deform under a compressive load. The purpose of this study was to use X-ray microtomography to examine the precise mechanisms by which an irregular flexible foam material deforms under compression.

It is well understood that the deformation of open-cell foams shows three main regimes: an initial linear elastic regime, where the strain energy is stored in the reversible bending of the struts, a plateau regime, where small increases in load lead to very large additional strain, and finally a densification regime where struts begin to impinge upon each other. At this last stage, the foam starts to exhibit a modulus approaching that of the solid material from which it is made. A schematic of the stress-strain curve for the uniaxial compression of an open-cell, flexible foam, showing the three regimes, is shown in Fig. 1.

Current theories for the shape of the load deflection curve of open-celled foams are based on the distinction between strut bending and strut buckling. It is commonly claimed [1] that the initial linear elastic part of the stress-strain curve is the result of the bending of struts which are oriented perpendicular to the load direction, while the plateau region of the stress-strain curve is the result of the 'buckling' of struts that are oriented parallel to the load direction. However, this reasoning is not relevant to the appearance of a plateau because the Euler buckling criterion only predicts the

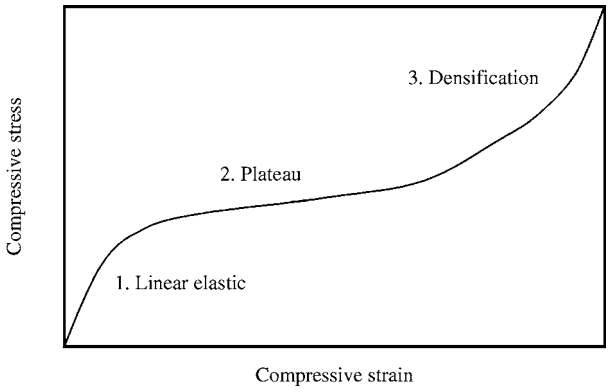

Figure 1 Schematic of a stress-strain curve for an open-cell flexible polyurethane foam, showing three deformation regimes: linear elastic, plateau and densification.

point at which a strut becomes less stiff than the bulk material. Moreover, the stress in the struts continues to rise as they buckle to higher deflections, so there is no justification for an overall collapse of the structure.

An alternative hypothesis to explain the existence of a plateau is that there are a series of local collapses that percolate through the structure at some critical stress, leading to 'bands' of high strain throughout the material. Such bands are well documented in the literature for metallic foams [2, 3] and have been observed perpendicular to the direction of applied stress for polymer foams [4, 5]. In this work we examine in detail the three-dimensional deformation mechanisms in all three regimes of the stress-strain curve, and propose a qualitative mechanism to account for the shape of the curve in irregular flexible foams.

1.2. X-ray absorption tomography

There are several experimental techniques that may be used to examine flexible foams in three-dimensions. The main techniques are confocal microscopy [6, 7], magnetic resonance imaging (MRI) [8, 9] and X-ray tomography [8].

Hamza *et al.* [6] have used confocal microscopy to image the deformation of a flexible foam. The main limitation of the optical approach is that it may only be used to image a shallow region of the material near to an exposed surface. The depth of the imaged region is limited by the fact that struts lying near the surface obscure those lying beneath. The effective depth that can be imaged is thus of the order of a single cell diameter. The technique is thus severely affected by edge effects since the imaged volume lies solely at the edge of the sample.

On the other hand, the use of MRI for determining structure in foams is somewhat limited by the contrast afforded by this technique. In order to enhance the contrast, workers in this field have chosen to fill the foams with a liquid penetrant such as water. Even with this contrast enhancement, imaging times are of the order of days and the spatial resolution that can be achieved is rather poor. Moreover, filling a flexible foam with an incompressible fluid will have an enormous effect on the stress-strain behaviour, and so MRI is unsuitable for deformation studies.

The principle of X-ray absorption tomography is to reconstruct the spatial distribution of the linear attenuation coefficient within the object from X-ray radiographs recorded at different angular settings of the sample. Each element in the recorded projections corresponds to a line integral of the attenuation coefficient along the beam path [10]. The 3D distribution of the attenuation coefficient can be calculated by a standard filtered back-projection algorithm that combines the information from different angular positions [11]. Since the attenuation coefficient is directly proportional to density for a given material, the technique effectively allows the elucidation of the three dimensional density distribution in the sample.

An additional feature that has been exploited here is the possibility to perform "local area" tomography. In this case, the sample is larger than the field of view and the projections are therefore truncated. The reconstruction is not exact, as high frequency noise can be produced, but it corresponds qualitatively well to the inner part of the larger sample. This approach is particularly attractive for studying foam compression since the imaging is performed in a region that is completely surrounded by foam and so the imaged deformation may be considered to be a true bulk deformation with artifacts due to the edges of the sample being effectively eliminated.

2. Method and materials

2.1. Materials

The subject of this study is a water blown MDI-based flexible polyurethane foam produced on a slab stock machine. The soft segment part of the formulation is a tri-functional 15 wt% ethylene oxide tipped poly(propyleneoxide) polyol. The overall molecular weight of the polyol is 6000 g mol^{-1} (Arcol 1374). The hard segment content of the polymer is 35.5 wt%. Additional foam expansion to 19.3 kg m^{-3} was achieved by injecting 3.5 wt% liquid CO_2 in the mixing head of the slab stock machine thus producing a foam bun with very low density and low hardness. This particular foam was selected because of its rather coarse but even cell structure. The sample which was studied had a microstructure typical of this type of foam.

Fig. 2(i) shows a scanning electron microscope image of a cut surface of the foam, with the rise direction horizontal. This image should be compared with that in Fig. 2(ii), which shows a different region of the same sample imaged using the X-ray tomography method, with the rise direction also horizontal. It is clear that the X-ray method gives an accurate representation of the foam texture. The curvature of the struts is easily seen and even the tricuspid profile of the struts may be clearly resolved. The apparent ribbed patterning on the tomographic image is an artifact of the image reconstruction algorithm.

The loading and unloading curves for a foam sample taken from the same block as the sample that was imaged are given in Fig. 3, with the compression axis parallel to the rise direction. The points at which tomographic images were collected are marked on the loading curve. These points were distributed with the

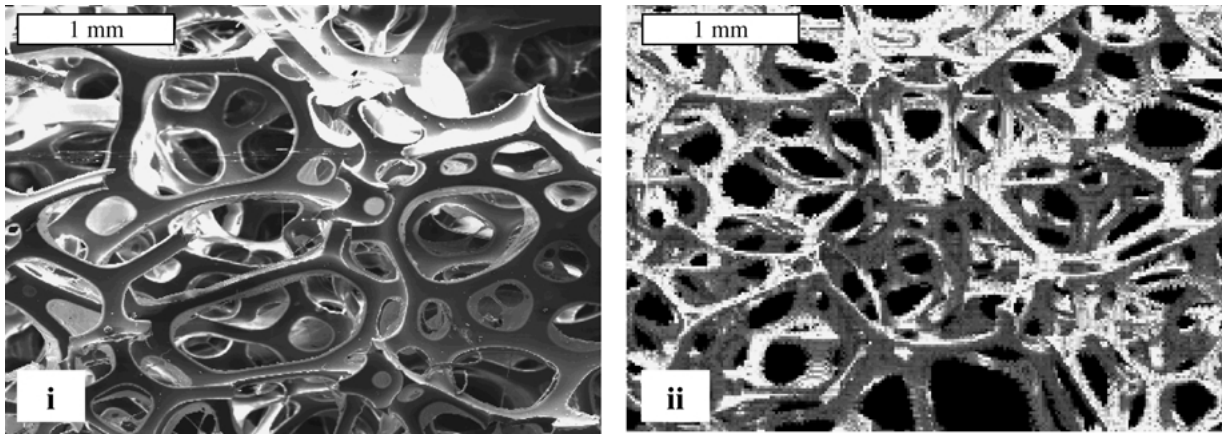

Figure 2 (i) SEM image of cut surface of polyurethane foam and (ii) reconstructed local area X-ray tomograph of a different region of the same sample. The rise direction is horizontal in both images.

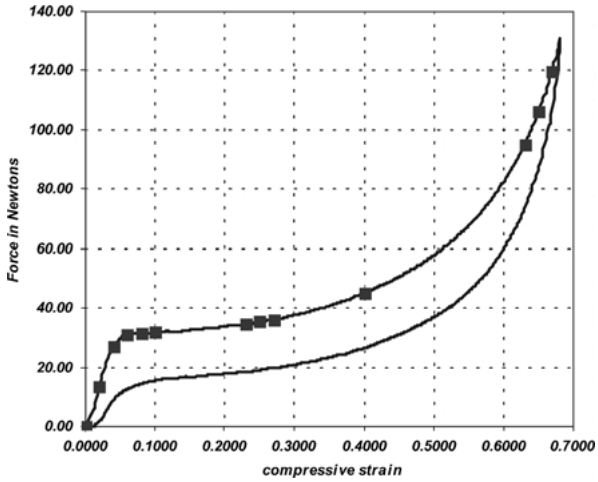

Figure 3 Loading/unloading deflection curve for a sample of the foam imaged. The dimensions of the sample for the loading measurements were 195 mm × 197 mm × 49 mm, with the rise direction vertical. The compression axis was parallel to the rise direction. The points indicated on the loading curve are the locations where tomographic images were obtained (0%, 2%, 4%, 6%, 8%, 10%, 23%, 25%, 27%, 40%, 63%, 65%, 67%). An additional image was recorded at 80% compression.

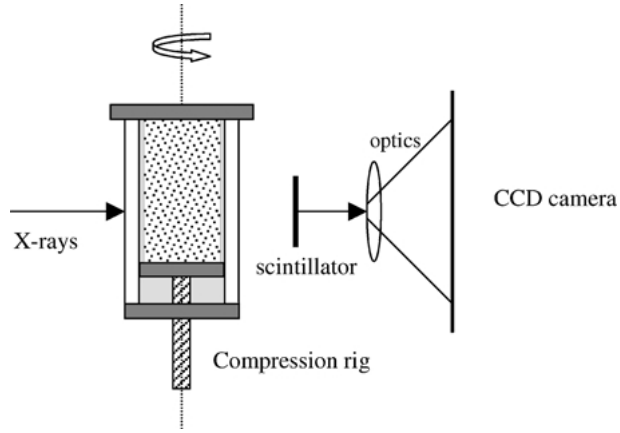

Figure 4 Schematic of experimental arrangement for collecting tomographs of compressed foam. The foam sample is enclosed by a Perspex cylinder and is compressed from below by a plunger attached to a calibrated stepper motor. The whole cylinder rotates on its axis during the experiment to allow collection of the tomographs.

intention of sampling each of the three deformation regimes described in the introduction. It was decided to cluster the points in each regime so that individual strut deformation processes could be followed between the samples.

2.2. Compression rig

The cylindrical foam sample, 25 mm in diameter and height, was compressed inside a highly polished Perspex tube, with internal diameter of 25.8 mm and with wall thickness of 0.25 mm, by a plunger driven by a stepper motor. The control of this stepper motor was integrated with the electronics of the beamline. This system of advanced control allowed fully automated tomographic scans of each foam sample at the different levels of compression. The high level of automation facilitated the collection of 14 complete data sets without user intervention over a period of approximately 18 hours.

2.3. Experimental arrangement

The experiments were carried out at the ID19 beamline of the European Synchrotron Radiation Facility (ESRF) in Grenoble, France. This beamline is devoted to high resolution imaging and features an energy tunable, parallel X-ray beam of up to 14×40 mm^2 cross-section (energy range: 7–100 keV, divergence 1 μrad). The compression rig was mounted on a precision mechanics sample stage (rotation and translation) and the projections were recorded with a fast, high-resolution detector system. The latter consists of a powder phosphor screen that is coupled via light optics to a cooled, low noise, 1024 by 1024 pixel CCD camera. A schematic of the setup, including the compression rig described in the preceding section, is shown in Fig. 4.

For this experiment, an effective pixel size of 6.6 μm proved best suited for the need to resolve the fine struts of the imaged foam whilst keeping a sufficiently large field of view in order to observe a statistically significant number of foam cells during the deformation process. The X-ray energy was adjusted to 9 keV using a Si-111 double crystal monochromator, resulting in optimum contrast for the weakly absorbing foam material. Typical exposure times for a single radiograph in this configuration were of the order of a few seconds.

2.4. Experimental procedure

In general, tomographic reconstruction requires that the lateral dimension of the object (perpendicular to the

rotation axis) does not exceed the field of view. However, this would have restricted the sample size to about 6 mm in diameter, thus increasing the influence of the sample surface and leading to problems due to sample bending during compression.

A different approach was adopted, using a relatively large sample diameter (25 mm) and performing local tomography of a small region close to the center. The foam sample was imaged at 14 levels of compressive strain (0, 2%, 4%, 6%, 8%, 10%, 23%, 25%, 27%, 40%, 63%, 65%, 67% and 80%). The foam sample was compressed parallel to the direction of rise. For each level of compression, 800 projection images spanning 180 degree rotation around the vertical axis were recorded. The time taken for each scan was around 1 hour. The reconstructions were performed offline using a standard filtered back-projection algorithm provided by Dr. F. Peyrin at the ESRF. The 3D volume data was rendered within the AVS/Express visualisation package [12].

After reconstruction of the 3D distribution of the linear attenuation coefficient, the data for the undeformed foam (i.e. at 0% strain) were skeletonised to produce a node-strut representation consisting of the node coordinates and a connectivity list. The raw volume data were processed using morphological filtering techniques [13] using a program written by S. Bouchet at the ESRF. The procedure was to impose a binary threshold on the volumes, followed by a morphological opening to eliminate small unconnected areas, and finally a morphological closing, to smooth the surface of the reconstruction. The output was then skeletonised by computing the Euclidean distance transform metric and calculating the geodesic perceptual graph [14].

3. Results and discussion

3.1. Tomographic imaging of foam deformation

Each volume data set consists of 1024 voxels cubed, with each voxel being 6.6 μm cubed. The images show 3D rendered images from the total volume data that are 256 voxels deep and 1024 voxels by 1024 voxels square. This corresponds to an actual volume of 1.7 mm by 6.8 mm by 6.8 mm, or 78.6 mm^3. The rendered volumes for selected levels of deformation are shown in Fig. 5.

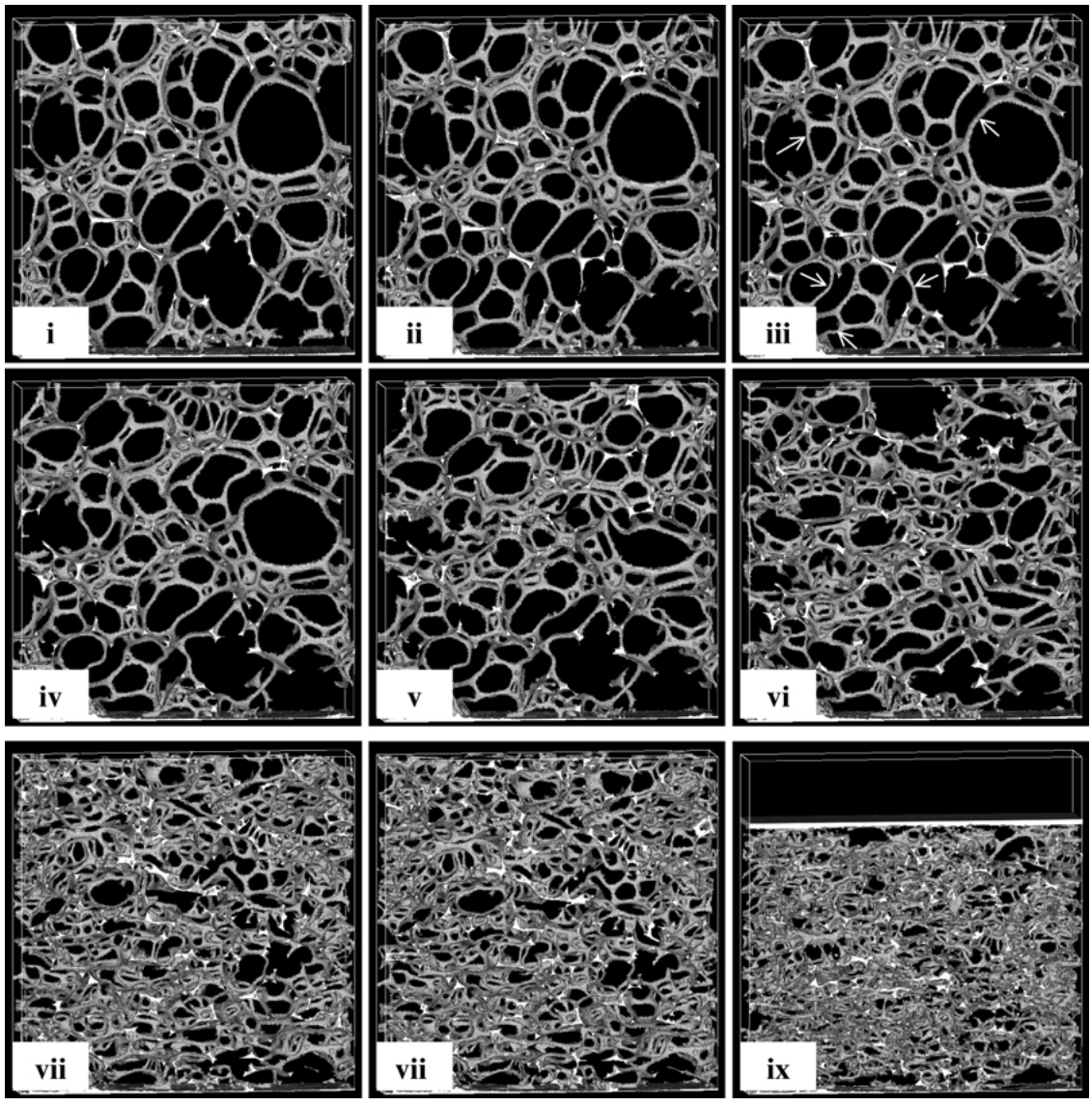

Figure 5 Selected X-ray tomographic images of the deformed polyurethane foam as a function of compressive strain: (i) 0%, (ii) 2%, (iii) 4%, (iv) 10%, (v) 23%, (vi) 40%, (vii) 63%, (viii) 65% and (ix) 80%. The bottom of these images corresponds to the fixed (upper) plunger in the experimental arrangement.

Confirmation of the size of the imaged volume may be obtained by a consideration of the final image, shown in Fig. 5(ix), at 80% compression where the plunger enters the field of view. The plunger appears at nearly three-quarters of the height of the image, consistent with the original sample dimension of 25 mm compressed by 80% to a height of just 5 mm.

Comparing the images at 0%, 2% and 4% strain (Fig. 5(i–iii)) clearly shows that the initial stages of the compression are taken up by small amounts of bending in struts that are longer than the average, and which are also inclined to the compression direction. Some examples of bent struts are marked by white arrows in Fig. 5(iii). Instead of observing struts that are perpendicular to the load direction bending, as described in existing models of foam deformation, we observe here that struts at various angles to the load direction are deformed. This corresponds to the linear elastic regime of the macroscopic stress-strain curve shown in Fig. 2.

Comparing the images at 10% and 23% strain (Fig. 5(iv) and (v)), it is clear that the next stage of the deformation process takes place by more severe bending of the longer struts. It is not that struts parallel to the loading direction suddenly exceed a critical 'buckling' stress, but rather that more severe bending of the struts occurs at this point due to cooperative bending and rotation of neighbouring struts. We believe that the images presented here show evidence for a collapse band. Careful comparison of the images at 10% strain (Fig. 5(iv)) and 23% strain (Fig. 5(v)) show that an entire band of cells have undergone severe distortion while other parts of the structure are almost unaffected by the increase in overall load. We believe that the mechanism of foam deformation is more accurately described by a cooperative bending and reorientation of a whole band of struts, and it is this transition to a cooperative 'collapse' that occurs at the knee in the stress strain curve, rather than a buckling transition in those struts that are aligned perfectly parallel to the load direction.

Comparing the images at 23% and 40% strain (Fig. 5(v) and (vi)) the collapse becomes more general throughout the structure. By 63% strain (Fig. 5(vii)), the struts begin to impinge on each other, and the deformation is clearly in the densification regime. At 80% strain (Fig. 5(ix)), the structure is very densely packed and it becomes difficult to resolve individual struts.

We have quantified the spatial homogeneity of the deformation in the three regimes of the stress-strain curve by calculating the relative displacement of signature peaks and troughs in the density profile averaged over planes perpendicular to the compression axis. For example, the average density profiles at 10% and 23% strain are plotted in Fig. 6. It can be seen that there is little change in the density profile from $z = 1$ to 150 from 10% (Fig. 6(i)) to 23% (Fig. 6(ii)) strain, but a large shift in the region $300 > z > 250$. By measuring the percentage displacement of similar peaks and troughs, and the integrated area (i.e. density) between them, it is possible to construct a displacement map of the microscopic strain in the sample due to the applied macroscopic strain.

The displacement map for the transition from 0% to 4% strain, which is in the linear elastic regime, is shown

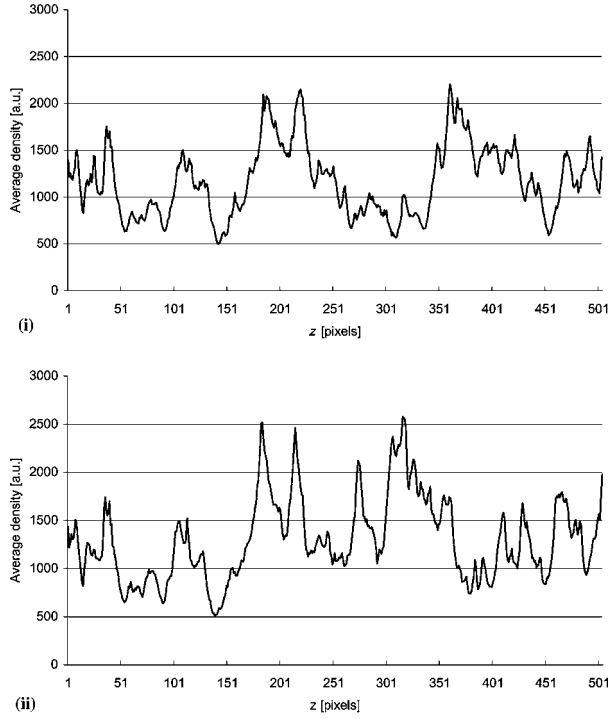

Figure 6 Density profiles from X-ray tomographs of polyurethane foam at (i) 10% and (ii) 23% strain, averaged in the plane parallel to the compression (z) axis.

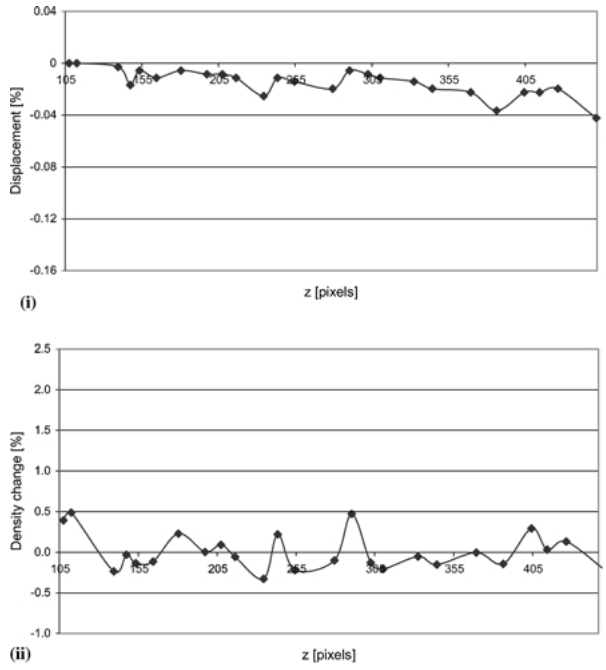

Figure 7 (i) Displacement of control points and (ii) change in integrated density between adjacent control points for polyurethane foam deformed from 0% to 4% compressive strain.

in Fig. 7(i). As expected, the microscopic strain was almost homogeneous, with some small fluctuations about a linear compressive trend. The overall microscopic strain was 4.2%, which is very similar to the nominal macroscopic strain of 4%. The integrated density between adjacent control points, given in Fig. 7(ii), shows a series of apparently uncorrelated expansions and contractions associated with the homogenous compression.

This behaviour should be contrasted against that observed in the plateau regime for the transition from

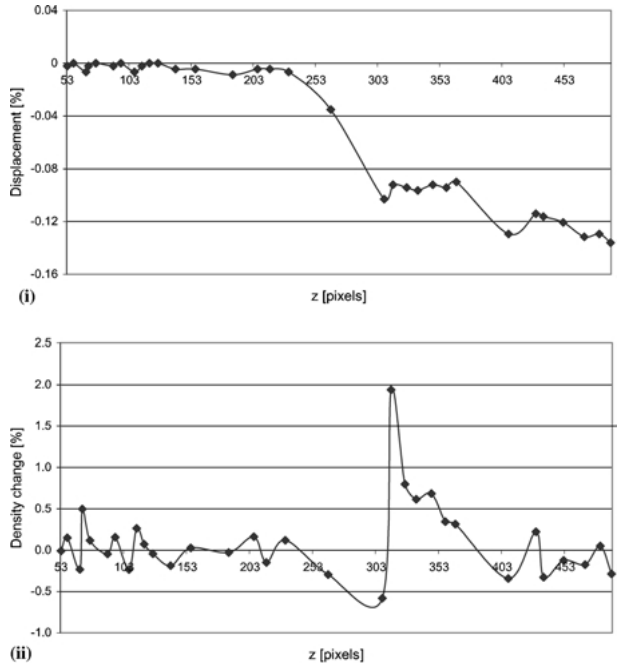

Figure 8 (i) Displacement of control points and (ii) change in integrated density between adjacent control points for polyurethane foam deformed from 10% to 23% compressive strain.

10% to 23% strain, shown in Fig. 8. In Fig. 8(i), which shows the displacement of the control points, the compression appears to be taking place mainly in discrete bands of the foam, between $230 < z < 300$ and $360 < z < 430$, with other regions of the foam deforming only very slightly. The bands of compression are preceded (plunger moves from large to small z) by sharp peaks in the integrated density, shown in Fig. 8(ii), indicating that the contractions are associated with localised densification of the foam. The overall microscopic incremental strain is 13.6%, which is very similar to the nominal macroscopic incremental strain of 14.4% (in going from 10% to 23% total strain). However, the microscopic strain is inhomogeneously distributed through the foam.

The inhomogeneous character of the deformation may be clearly observed in the tomographic reconstructions corresponding to 10% and 23% strain, shown in Fig. 9(i) and (ii) respectively. The main strain band is associated with the collapse of the cells marked A–E. It appears that a group of connected cells simultaneously becomes unable to support the compressive stress and therefore collapses to form a band of denser material. The collapsed bands need not necessarily run perpendicular to the deformation direction, although there is a tendency for them to do so because this is the direction of greatest resolved bending stress on the struts.

Once the foam has been compressed sufficiently for the collapsed bands to impinge on each other, the foam enters the densification regime where the microscopic deformation is once again homogeneous. This is shown in Fig. 10, for the transition from 63% to 65% strain. The overall microscopic incremental strain is 4.9%, which is very similar to the nominal incremental macroscopic strain of 5.4% (in going from 63% to 65% total strain). It was not possible to follow the deformation process microscopically between the plateau and densification regimes, due to the difficulty in identifying common sections of foam from the density profiles, and therefore we cannot rule out the possibility of further collapse bands forming in this transition region. However, as far as we can determine from the current data, the microscopic deformation appears to be homogeneous.

3.2. Node-strut models of foams

The results of the skeletonisation procedure described in the methods section are shown for a subset of the volume data in Fig. 11. In general, the correspondence between the filtered tomographic image (Fig. 11(i)) and node-strut model (Fig. 11(ii)) is good, although there

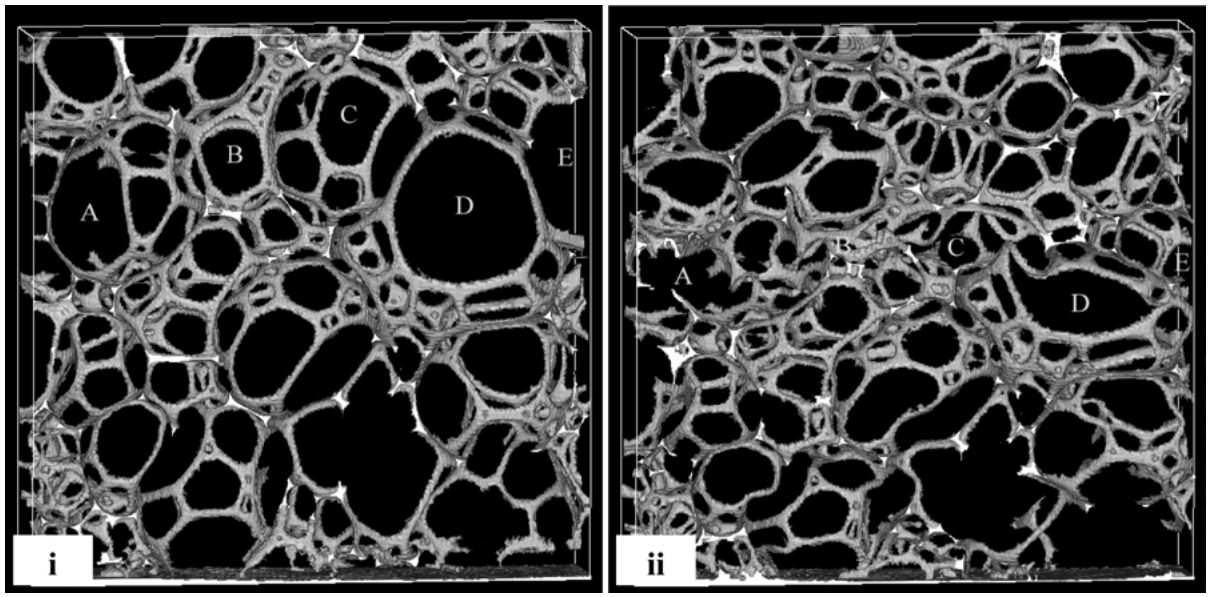

Figure 9 X-ray tomographic images showing the formation of a collapsed band in deformed polyurethane foam at (i) 10% and (ii) 23% compressive strain. The cells marked A–E are the same in each image.

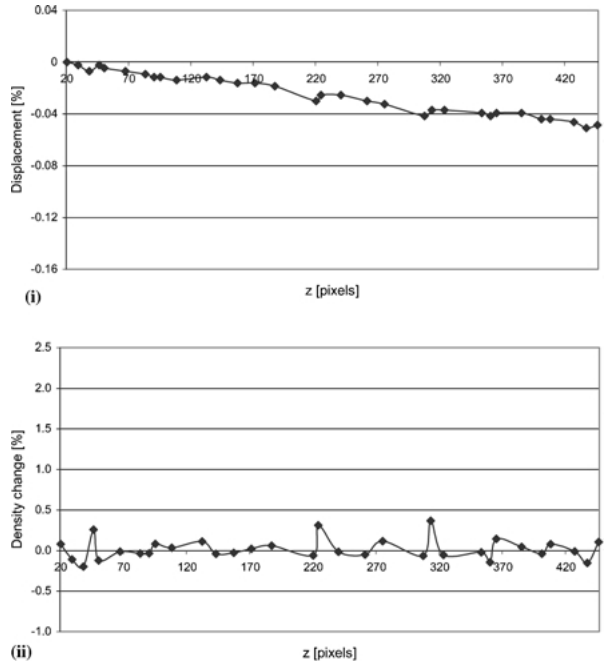

Figure 10 (i) Displacement of control points and (ii) change in integrated density between adjacent control points for polyurethane foam deformed from 63% to 65% compressive strain.

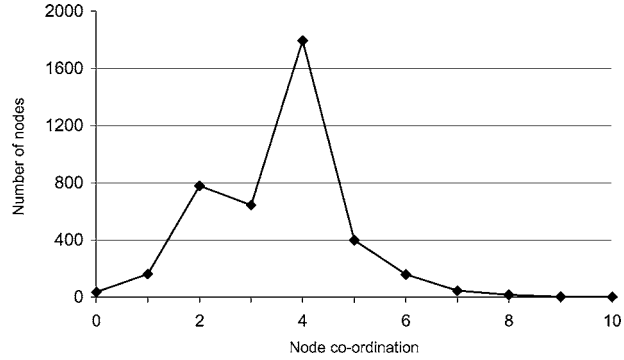

Figure 12 Node coordination distribution for 1024 voxel cubed foam derived from skeletonised node-strut model.

are a number of systematic discrepancies that require some explanation. Most significantly, the node-strut model can only incorporate straight struts, and therefore curved struts in the tomographic data are replaced by a series of connected straight struts after skeletonisation. This will obviously affect the elastic properties of the derived node-strut model, and means that the node-strut model is ill-suited to describe deformed samples. Another feature, which is somewhat related to the mass density of the foam studied, is that areas of solid polymer are replaced by multiple struts. In particular, certain nodes have been replaced by a tetrahedral arrangement of nodes and struts. In some cases this is justified by the tomographic data, and in other cases not. In any case, we do not believe it will have any significant effect on the local elastic properties. Using the node-strut model, the node coordination, strut length and cell size distributions for the entire foam (1024 voxels cubed) were extracted. The node coordination distribution is shown in Fig. 12, and the strut length and cell size distributions in Fig. 13. The results show that the modal coordination of the nodes was 4, as expected for a 3-dimensional foam of low surface energy, with the mean coordination being slightly lower at 3.5. There is an anomalous peak at a coordination of 2, which is an artifact of the skeletonisation algorithm in that some curved struts are detected as a pair of straight struts with a node of coordination 2 connecting them.

The modal strut length was approximately 0.11 mm but with a long tail in the distribution, resulting in a mean strut length of around 0.25 mm. It is also apparent from the strut length distribution that there is a cut-off at low strut lengths. In fact the cut-off appears at a length that is commensurate with a strut diameter. This is really a simple geometric cut-off and lies in the fact that a strut must be longer than its own diameter. The fact that the cut-off seen here is not sharp is a result of the fact that the node detection algorithm sometimes

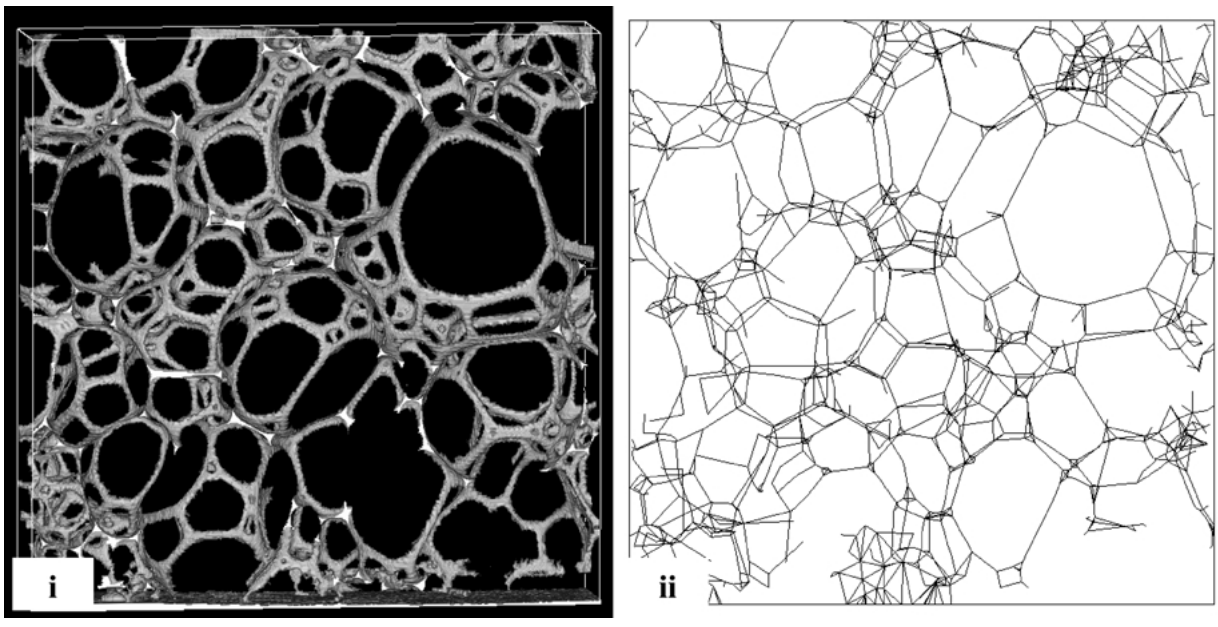

Figure 11 (i) Morphologically filtered X-ray tomograph and (ii) corresponding node-strut model of a section of the undeformed polyurethane foam.

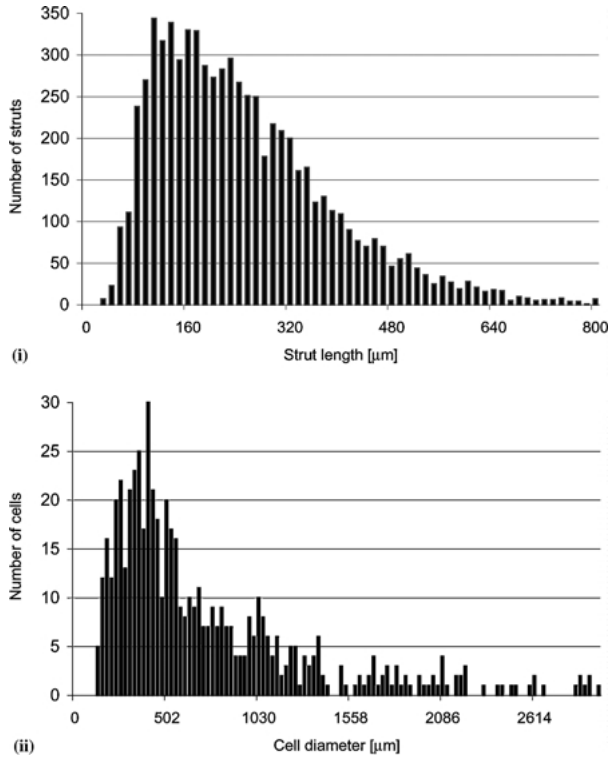

Figure 13 (i) Strut length and (ii) cell size distributions for 1024 voxel cubed foam derived from skeletonised node-strut model.

finds two nodes within the same proximity, and then a short strut is found connecting them. An improvement to the algorithm would consist in grouping these nodes together as a single node. The cell size distribution, which was found by obtaining spheres of best fit to each cell in the node-strut model, is shown in Fig. 13(ii). The modal cell diameter was 0.42 mm but, as with the strut length distribution, a long tail resulted in a mean diameter of 0.75 mm.

One of the motivations for this work was to try to use detailed X-ray tomography measurements of foam deformation to help validate finite element models of foam deformation. In these models [15, 16] foams are treated as networks of slender struts joined at tetrahedral junctions. There are a number of issues still to be resolved before these experimental and modelling approaches can be fully integrated. An important aspect of the modelling work is that a bulk system can only be achieved by imposing periodic boundary conditions, in which each edge of the finite sized model wraps around to the opposite edge allowing an effectively infinite structure to be modelled. A naïve approach to seeking agreement between the modelling results and the experimental measurements presented here would be to take the observed strut network and simply import this structure into a finite element code. However this procedure suffers from the major drawback that opposing pairs of edges cannot be matched to provide periodic boundaries. The boundary conditions have such a profound effect on the elastic properties that a true comparison cannot currently be made with the real foam structures. In the future it is planned to overcome these issues by constructing *ab initio* periodic foams with cell size and strut length distributions that match the experimental foams.

4. Conclusions

An open-cell flexible polyurethane foam was imaged *in situ* at a range of compressive strains using local area X-ray microtomography. The images from the undeformed sample were in good agreement with corresponding SEM micrographs, demonstrating that the tomographic technique can provide an accurate representation of the internal structure of the foam. The deformation process was shown to occur homogeneously throughout the foam up to a compressive strain of around 6%, at which point locally collapsed bands of denser material began to form, corresponding with a dramatic loss of stiffness in the macroscopic stress-strain curve. From the tomographic images, it was possible to see the formation of a collapse band around a particular foam cell that was rather larger than its immediate neighbours. However, this was not an isolated buckling transition, but rather a cooperative collapse through an entire layer of connected cells of considerable extent.

As the amount of material in the collapsed bands increased, the deformation was observed to become homogeneous again as the bands began to impinge on each other. An attempt was made to construct a node-strut model of the undeformed sample, in order to compare the deformation processes observed using tomography with finite element modeling. Although the node coordination, strut length and cell size distributions could be determined, it was not possible to simulate the deformation process due to the lack of information about the boundary conditions of the sample, which have a profound influence on the elastic properties.

Acknowledgments

The authors are grateful to Dr. Françoise Peyrin of the ESRF for providing the software 'VOLUMIC' with which the 3D tomographic reconstructions were made. They would also like to thank Sebastien Bouchet for writing the morphological filtering program. Also, Perttu Niemelä for his algorithm to fit spheres to skeletonized data.

References

1. L. J. GIBSON and M. F. ASHBY, "Cellular Solids" (Pergamon Press, Oxford, 1988).
2. W. J. STRONGE and V. P. W. SHIM, *J. Eng. Mat.* **110** (1988) 185.
3. S. D. PAPKA and S. KYRIAKIDES, *J. Mech. Phys. Solids* **42** (1994) 1499.
4. R. LAKES, P. ROSAKIS and A. RUINA, *J. Mater. Sci.* **28** (1993) 4667.
5. Y. WANG, G. GIOIA and A. M. CUITIÑO, *J. Eng. Mat. Tech. ASME* **122** (2000) 376.
6. P. D. THOMAS, R. C. DARTON and P. B. WHALLEY, *Ind. Eng. Chem. Res.* **37** (1998) 710.
7. R. HAMZA, X. D. D. ZHANG, C. W. MACOSKO, R. STEVE and M. LISTEMANN, *ACS Sym. Ser.* **669** 165 (1997).
8. M. SZAYNA and R. VOELKEL, *Solid State Nucl. Mag.* **15** (1999) 99.
9. B. J. PANGRLE, B. E. HAMMER, N. P. BIDAULT, M. L. LISTEMANN, R. E. STEVENS, X. D. ZHANG and C. W. MACOSKO, in Expo 98, Dallas, 1998 p. 247.

10. J. RADON, *Ber. Verh. Sächs. Akad. Wiss. Leipzig Math. Phys. Kl.* **69** (1917) 262.
11. G. T. HERMAN, "Image Reconstruction from Projections. Computer Science and Applied Mathematics" (Academic Press, New York, 1980).
12. Advanced Visual Systems, 300 Fifth Avenue, Waltham, MA 02451, USA.
13. R. M. HARALICK, S. R. STERNBERG and X. H. ZHUANG, *IEEE T. Pattern Anal.* **9** (1987) 532.
14. F. MEYER, *Signal Process.* **16** (1989) 335.
15. H. X. ZHU, J. R. HOBDELL and A. H. WINDLE, *Acta Mater.* **48** (2000) 4893.
16. *Idem.*, *J. Mech. Phys. Solids* **49** (2001) 857.

Received 17 April
and accepted 21 September 2001